

# Effect of spin-dependent tunneling in a $\text{MoSe}_2/\text{Cr}_2\text{Ge}_2\text{Te}_6$ van der Waals heterostructure on exciton and trion emission

Annika Bergmann-Iwe,<sup>1</sup> Swarup Deb,<sup>1,2,3</sup> Klaus Zollner,<sup>4</sup> Veronika Schneidt,<sup>1</sup> Mustafa Hemaïd,<sup>1</sup> Kenji Watanabe,<sup>5</sup> Takashi Taniguchi,<sup>6</sup> Rico Schwartz,<sup>1</sup> Jaroslav Fabian,<sup>4</sup> and Tobias Korn<sup>1,\*</sup>

<sup>1</sup>*Institute of Physics, Rostock University, 18059 Rostock, Germany*

<sup>2</sup>*Saha Institute of Nuclear Physics, Kolkata, India*

<sup>3</sup>*Homi Bhabha National Institute, Mumbai, India*

<sup>4</sup>*Institute for Theoretical Physics, Regensburg University, 93040 Regensburg, Germany*

<sup>5</sup>*Research Center for Electronic and Optical Materials, NIMS, 1-1 Namiki, Tsukuba 305-0044, Japan*

<sup>6</sup>*Research Center for Materials Nanoarchitectonics, NIMS, 1-1 Namiki, Tsukuba 305-0044, Japan*

We study van der Waals heterostructures consisting of monolayer  $\text{MoSe}_2$  and few-layer  $\text{Cr}_2\text{Ge}_2\text{Te}_6$  fully encapsulated in hexagonal Boron Nitride using low-temperature photoluminescence and polar magneto-optic Kerr effect measurements. Photoluminescence characterization reveals a partial quenching and a change of the exciton-trion emission ratio in the heterostructure as compared to the isolated  $\text{MoSe}_2$  monolayer. Under circularly polarized excitation, we find that the exciton-trion emission ratio depends on the relative orientation of excitation helicity and  $\text{Cr}_2\text{Ge}_2\text{Te}_6$  magnetization, even though the photoluminescence emission itself is unpolarized. This observation hints at an ultrafast, spin-dependent interlayer charge transfer that competes with exciton and trion formation and recombination.

## I. INTRODUCTION

In recent years, two-dimensional (2D) crystals and van der Waals (vdW) heterostructures [1] consisting of different 2D crystals have been one of the most active fields in solid-state research. Besides graphene, the semiconducting transition metal dichalcogenides (TMDCs) such as  $\text{MoSe}_2$  have garnered a lot of research attention. This is due to their exciting electronic and optical properties. In the monolayer (ML) limit, they become direct-gap semiconductors [2] with a peculiar band structure leading to spin-valley coupling [3]. These properties make them potentially interesting for spintronics [4] and valleytronics [5], where information is encoded in the spin or valley degree of freedom of carriers, instead of their charge. In ML TMDCs, the optical selection rules allow generation of a coupled spin-valley polarization of excitons using circularly polarized excitation, and the excitonic valley polarization degree can be read out directly in helicity-resolved photoluminescence (PL) measurements [6, 7]. Depending on the specific TMDC material, this mechanism for generating a valley polarization can be very effective and robust, even for highly nonresonant excitation.

For the specific case of  $\text{MoSe}_2$ , however, the valley relaxation rate is extremely fast compared to that of exciton recombination, so that a significant circular polarization of the PL emission can only be observed for near-resonant excitation [8–10]. Despite the unfavourable relaxation rates, an excitonic valley polarization can be achieved by lifting the energy degeneracy of opposite valleys. A usual strategy has been to exploit external magnetic fields perpendicular to the plane of a TMDC ML

to break time-reversal symmetry. This introduces a valley Zeeman splitting and leads to a preferential occupation of the energetically favorable valley, even for unpolarized and nonresonant excitation [11, 12]. However, the effective g factors for TMDC monolayers correspond to a splitting of only about 0.2 meV per Tesla, so that magnetic fields of several Tesla are required to achieve a significant valley polarization even at liquid helium temperature.

As such field strengths are impractical for device applications, the use of magnetic proximity effects [13], where the proximity of a magnetic material induces a magnetization through exchange interaction, has been explored in recent years. This has made it possible to tailor the spin-valley properties in TMDCs without the need for an external magnetic field [14]. Alternatively, spin injection from ferromagnetic materials was used to generate valley polarization in TMDCs [15]. A variety of bulk ferromagnetic materials ranging from metals like Nickel [16] to ferromagnetic semiconductors such as  $\text{Ga}(\text{Mn})\text{As}$  [15] and  $\text{EuS}$  [17] were employed in experimental studies. However, the presence of surface states, dangling bonds, interface reconstruction, etc. greatly complicates their integration into vdW heterostructures.

For this, layered ferromagnetic materials [18, 19], made of chemically stable atomically thin sheets, have recently emerged as a viable alternative for integration into vdW heterostructures. While there have been a number of experimental studies [14, 20–22], among the plethora of available TMDC and vdW ferromagnets, it remains elusive which material combinations, thicknesses, and other parameters offer the best material platform for studying phenomena such as spin-dependent tunneling and magnetic proximity effects.

Here, we report on an optical spectroscopy study of vdW heterostructures consisting of monolayer  $\text{MoSe}_2$  and the ferromagnetic semiconductor  $\text{Cr}_2\text{Ge}_2\text{Te}_6$  (CGT) [23, 24] encapsulated in hexagonal Boron Nitride (hBN). Low-

---

\* tobias.korn@uni-rostock.de

temperature photoluminescence measurements reveal a partial quenching of the PL and a significantly reduced trion-to-exciton emission ratio in the heterostructure as compared to an isolated  $\text{MoSe}_2$  ML, indicating an electron transfer from the  $\text{MoSe}_2$  into the CGT. Under nonresonant, circularly polarized excitation, we find that the exciton-trion ratio depends on the relative orientation of excitation helicity and CGT magnetization. Remarkably, this effect is observable even though the PL emission itself is unpolarized, indicating a vanishing valley polarization of excitons and trions. DFT calculations of the heterostructure predict a type-I band alignment and a pronounced spin splitting of the CGT conduction band, yielding a large spin-polarized density of states for interlayer electron tunneling. Based on this, we interpret our observations as an interplay of spin-dependent tunneling of the initially valley-polarized electrons from  $\text{MoSe}_2$  into CGT with exciton and trion formation, valley relaxation and recombination.

Our findings offer a glimpse into material combinations that can be utilized for spin generation and hosting, and more importantly, provide a potential means to read out spin polarization and light helicity through spin-selective tunneling - an essential component in the process and measurement chain of spin-valleytronic devices.

## II. RESULTS AND DISCUSSION

To begin with, we discuss the structure and characterization of our samples. As an example, Figure 1a shows a fully hBN-encapsulated  $\text{MoSe}_2/\text{CGT}$  heterostructure. Attached to bulk CGT, two thin CGT regions I and II of different thickness cover an underlying  $\text{MoSe}_2$  monolayer and are thus of particular interest. After exfoliation, optical images of the CGT flake were taken in transmission mode inside an inert gas glovebox used for sample preparation (see methods). From the absorbance in conjunction with AFM measurements, we estimate the CGT flake to consist of 14 layers in region I and of 9 layers in region II (see supplementary materials [25] Figure S1). Low-temperature PL measurements at 5 K were used to characterize the resulting heterostructure. The sample was scanned and the PL map depicted in Figure 1b was created using an automated routine that fitted the most intense peak in each spectrum with a Gaussian. Numerical integration of the energetic range containing both trion and exciton emission reveals a quenching by a factor of about five of the  $\text{MoSe}_2$  monolayer emission in the heterostructure region compared to the isolated  $\text{MoSe}_2$  monolayer, indicating a high-quality interfacial contact for interlayer charge transfer between both layers [26]. Maps to further characterize the exciton and trion emission as well as the exciton and trion peak energies can be found in Figure S2. Due to the CGT flake on top of the  $\text{MoSe}_2$  monolayer, which acts as an additional absorbing layer, the quenching is slightly overestimated. Exemplary spectra (Fig. 1c) illustrate that both trion and

exciton emission are suppressed in the heterostructure region, with trion emission being more strongly affected. Whereas trion emission dominates the isolated monolayer spectrum, the exciton-trion ratio is significantly larger in the heterostructure region. Whether either trion or exciton emission is more pronounced in the spectrum depends on the position on the heterostructure, which we attribute to locally different interface qualities due to inclusions between the two layers. A color map depicting the spatial distribution of exciton-trion ratios is shown in Figure S3.

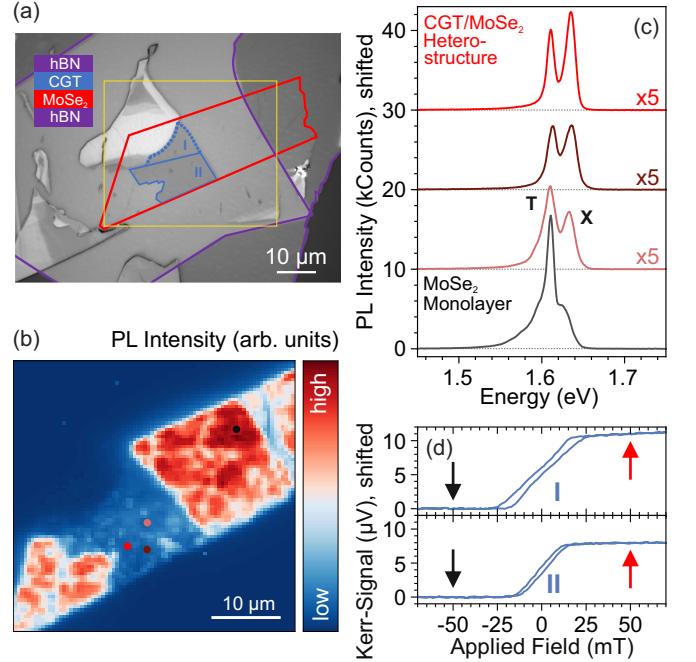


Figure 1. (a) Optical microscope image of an hBN-encapsulated  $\text{MoSe}_2/\text{CGT}$  heterostructure. A CGT flake with regions of various layer thickness (I) and (II) covers an underlying  $\text{MoSe}_2$  monolayer. The yellow box corresponds to the false color map of the PL scan area (b), showing quenching of the  $\text{MoSe}_2$  monolayer emission in the heterostructure region. (c) Compared to the  $\text{MoSe}_2$  monolayer the integrated PL emission is reduced by a factor of about five. In addition, the ratio of exciton (X) and trion (T) is increased in the heterostructure, with different exciton-trion ratios observed, depending on the measurement position. All spectra were taken from the PL scan. Their positions are marked by the colored dots corresponding to the color of the spectrum. (d) MOKE measurements prove ferromagnetic behavior of the CGT flake. Magnetic saturation is reached at 32 mT and 18 mT for I and II, respectively. The arrows indicate the applied field of  $\pm 50$  mT for the helicity-resolved measurements described below.

For further polarization-resolved PL measurements, a fully saturated magnetization along the out-of-plane axis of the CGT flake is crucial. This makes the magnetization (anti-)parallel to the spin orientation in the TMDC  $K$  valleys. Polar magneto-optical Kerr effect (MOKE) measurements at a nominal sample temperature of 5 K

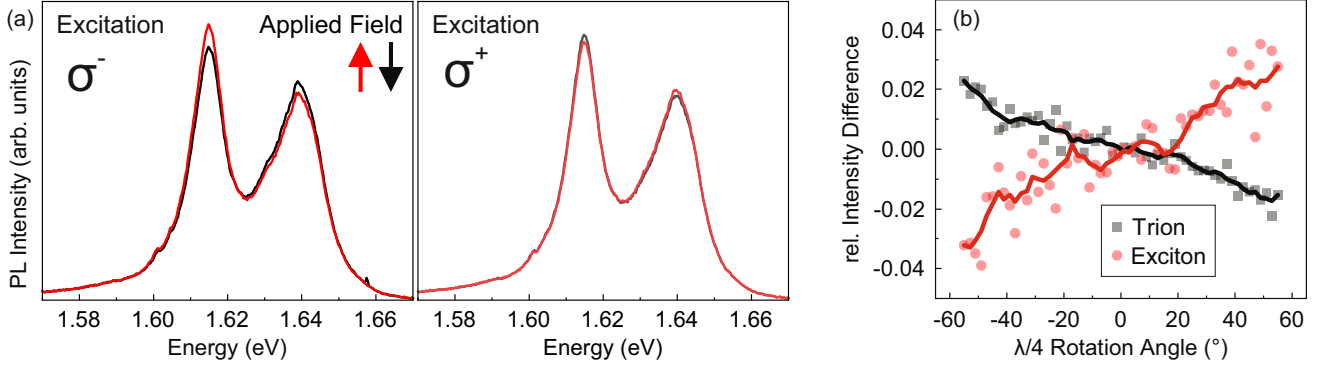


Figure 2. (a) Low-temperature PL spectra taken in the heterostructure region II in presence of an external magnetic field ( $\pm 50$  mT) for left ( $\sigma^-$ ) and right ( $\sigma^+$ ) circularly polarized excitation. For a fixed excitation helicity, trion and exciton intensities change in dependence of the magnetic field direction (arrows). (b) The relative intensity difference for exciton and trion upon flip of magnetic field depends on the degree of circularly polarized excitation, vanishing for linear polarization at a  $\lambda/4$  rotation angle close to  $0^\circ$ . The solid lines represents the sliding average of five data points and serve as guide to the eye. The data were collected in heterostructure region I. The maximum relative intensity differences observed are comparable to those in region II.

(illustrated in Figure 1d) show clear hysteresis loops for both heterostructure regions. As expected, the thinner region II shows a smaller Kerr signal range than the thicker region I. We observe a small remanence and low coercive field for region II. By contrast, we find a more complex, bow-tie-like shape of the hysteresis loop for the thicker region I, which resembles previous reports on hysteresis loops for CGT flakes thicker than 13 layers [27] or 10 nm [28], closely matching our thickness estimates based on absorbance. As a consequence of the small magnetic remanence observed in MOKE, all subsequent measurements were conducted at an external magnetic field of  $\pm 50$  mT, ensuring magnetization saturation parallel to the direction of the external magnetic field.

Valley polarization effects were investigated by nonresonant PL measurements using an excitation wavelength of 633 nm. Circularly polarized excitation was achieved using an achromatic quarter-wave-plate ( $\lambda/4$ -plate). A second  $\lambda/4$ -plate in conjunction with a linear polarizer was used for helicity-resolved detection. With a constant excitation helicity, multiple PL spectra were measured with alternating magnetic field direction. Spectra recorded at the same magnetic field direction were then summed up to improve the signal-to-noise ratio. This was repeated for the opposite excitation helicity. We emphasize that in these measurements the detection helicity was fixed. Remarkably, the population dynamics described below is observed irrespective of the detection helicity and can also be seen in linearly polarized detection (Fig. S4). Figure 2a shows evidence for magnetic-field-dependent changes of exciton and trion emission. The spectra measured at a spot in heterostructure region II show that for left-polarized ( $\sigma^-$ ) excitation populating the  $K^-$  valley, the trion intensity is larger when a positive (red) magnetic field is applied, compared to a negative (black) magnetic field of the same magnitude. The opposite trend is observed for exciton emission where a larger intensity is seen at a negative

magnetic field. In contrast, under right-polarized ( $\sigma^+$ ) excitation the intensity distributions for both trion and exciton are reversed. However, the magnetic-field-dependent intensity variation has a different magnitude for right and left circularly polarized excitation. We attribute this to a minor deviation from the optimum excitation helicity. In addition, a small beam offset induced by rotating the  $\lambda/4$ -plate can result in a slightly different excitation spot on the sample.

Qualitatively, the same effect occurs in heterostructure region I and is reproduced in another sample (see Fig. S5).

To quantify the normalized magnetic-field-induced intensity differences, we define them as:

$$\Delta I = \frac{I(B \downarrow) - I(B \uparrow)}{I(B \downarrow) + I(B \uparrow)} \quad (1)$$

where  $\downarrow \uparrow$  denotes the external magnetic field direction. Exciton and trion intensities were determined by numerical integration around the respective peak positions. Changing the degree of circular polarization by rotating the  $\lambda/4$ -plate in the excitation (Fig. 2b), demonstrates a vanishing intensity difference for linear excitation corresponding to an angle of about  $0^\circ$ , whereas an increasing difference occurs for excitation deviating from linear polarization, reaching maximum values of about 4%.

To confirm that the intensity differences result from an interaction between the  $\text{MoSe}_2$  monolayer and the magnetized CGT, the same measurement was performed on an isolated part of the monolayer. Here, the same trion (exciton) intensity was detected irrespective of the magnetic field direction for both left and right circularly polarized excitation (Fig. S5).

We note that we do not observe any discernible Valley Zeeman splitting in our helicity-resolved PL measurements, which were performed using applied magnetic fields of 50 mT, neither for the heterostructure nor for

the isolated MoSe<sub>2</sub>. Our experimental accuracy should allow us to resolve Valley Zeeman splitting on the order of 0.5 meV or above. This gives an upper limit for any proximity-effect-induced Valley Zeeman splitting effect present in our samples. Such values are well below those reported in previous studies [14, 22]. Our calculations yield a value of 3.7 meV in the single-particle picture based on the splitting of MoSe<sub>2</sub> conduction and valence bands (see Fig. S11). However, we note that the theory calculation is likely to overestimate the splitting as it requires crystallographic alignment of the TMDC and the CGT layers at a specific twist angle of about 16 degrees in order to obtain a reasonable supercell size for DFT calculations. By contrast, in the experiment, the alignment angle between the constituents of the heterostructure is optimized to yield large overlap of flake areas and alignment of straight edges, which is likely to result in twist angles close to zero degrees. Previous theory calculations on twist angle dependence have shown the magnetic proximity effect to be fragile and strongly dependent on interlayer twist [29, 30].

Based on work functions for both MoSe<sub>2</sub> monolayer and CGT flakes of the determined thickness [21], the heterostructure should possess a type I band alignment with the MoSe<sub>2</sub> conduction band being energetically higher than that of CGT, which is verified by DFT calculations. These are discussed in detail in the supplementary materials (See [25] and references therein [31–43]). The exciton and trion emission quenching in the heterostructure region compared to the isolated monolayer as well as the larger exciton-trion ratio in the heterostructure indicate electron transfer from MoSe<sub>2</sub> into CGT. This is visible in Figures S2a and S2c, as well as Figure 1c. In the latter, since the quenching is more pronounced for the trion, a shift of relative spectral weight towards the exciton is observed.

Predominantly, the exciton-trion ratio in the heterostructure is modulated by the following mechanisms: Electron transfer reduces the background carrier density in MoSe<sub>2</sub>, lowering the probability of trion formation, which leads to an increase in the exciton-trion emission ratio typical for TMDCs [44, 45]. Besides, trions in MoSe<sub>2</sub> have significantly longer photoluminescence lifetimes (15 ps) than excitons (2 ps) [8, 46], so that they are more susceptible to nonradiative decay channels, such as electron tunneling into the CGT, during their lifetime.

In addition to the common carrier density-dependent changes in PL intensity of exciton and trion, we observe a subtle helicity- and magnetic field-dependent modulation in the exciton-trion emission ratio, as shown in Figure 2. Interestingly, for a fixed excitation helicity, trion and exciton show opposite intensity changes when the magnetic field is flipped. We identify two main factors that explain this observation: (i) spin-dependent tunneling of electrons from MoSe<sub>2</sub>, which determines the quasi-equilibrium carrier concentration under photo-excitation and (ii) the exciton-trion conversion, which depends on excess carrier concentration, as well as on competing exciton and trion formation and recombination times.

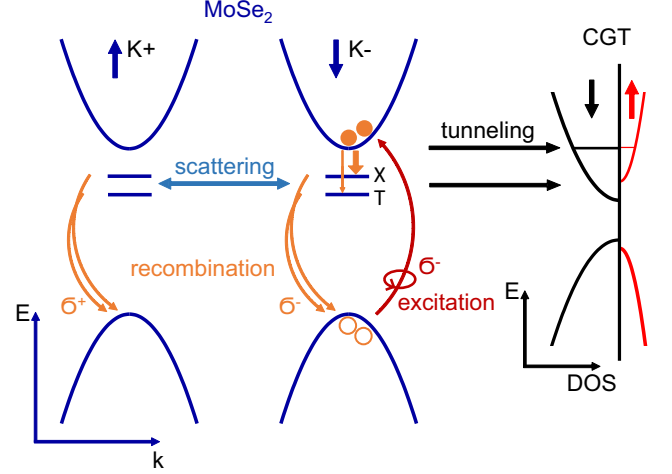


Figure 3. Illustration of processes causing the population dynamics for  $\sigma^-$  excitation and  $B \downarrow$ . Spin-down electrons in the  $K^-$  valley tunnel into the CGT due to a high density of available spin-down states in the conduction band. The decreased charge carrier density in MoSe<sub>2</sub> reduces the trion formation rate and a large fraction of excitons recombines radiatively. A change of magnetic field direction would result in a smaller density of spin-down states in the CGT, leading to increased trion formation at the expense of exciton recombination. The initial valley polarization is lost due to scattering between the valleys, causing the collected PL to stem from both valleys. The collected PL is thus irrespective of the detection helicity.

To explain the intricate interplay of these factors, we consider the behavior under left circularly polarized excitation ( $\sigma^-$ ), which selectively populates the  $K^-$  valley with spin-down electrons, as illustrated in Figure 3.

Due to the external magnetic field, the CGT flake is magnetically saturated with the spin states aligned with the external magnetic field direction. As evident from DFT calculations, a spin-dependent splitting of the CGT conduction band exists. For a negative magnetic field, the electrons residing in the  $K^-$  valley therefore encounter a high density of available spin-down states in the CGT conduction band. This increases the tunneling rate, which reduces the number of free spin-down electrons in the MoSe<sub>2</sub> conduction band. Interlayer charge transfer in TMDC heterostructures has been reported, depending on the material combination, to usually occur within 50 fs [47, 48]. Similar transfer rates can be expected for TMDC-CGT heterostructures. Whereas a considerable portion of excitons already forms within 0.4 ps after excitation [49], in parallel with interlayer charge transfer, trion formation in MoSe<sub>2</sub> monolayers takes place on a much slower timescale of 2 ps [50] and depends on the background carrier density. In the presence of a negative magnetic field, trion formation and subsequent recombination is thus suppressed as a result of the reduced availability of excess electrons in MoSe<sub>2</sub>. In parallel, we observe a higher exciton intensity at a negative magnetic



field. As trion formation and exciton recombination occur on similar timescales of about 2 ps [8, 34], a larger fraction of excitons recombines radiatively. In contrast, for a positive magnetic field, the tunneling rate for spin-down electrons is reduced, so that trion formation is enhanced and consequently a larger fraction of excitons is converted to trions before recombination.

Changing the excitation helicity to  $\sigma^+$  flips the spin compatibilities with the spin-split density of states in the CGT and thus reverses the behavior explained above. Therefore, the magnetic-field dependent differences of exciton and trion emission invert their sign, as observed in Figure 2b. Notably, the effect described above was reproduced in a second sample (Fig. S5), although there, measurement positions were also found where both trion and exciton emission were suppressed under conditions of high tunneling probabilities (Fig. S6). We attribute these distinct manifestations of the spin-selective tunneling process to differences in the relative rates of the processes involved, highlighting the sensitivity of the sample system to local changes.

At this point, it shall again be highlighted that the overall detected PL emission is unpolarized. We ascribe this to intervalley scattering mediated by long-range Coulomb interaction [51] which was identified to be the main mechanism for exciton valley depolarization after initial circular excitation in MoSe<sub>2</sub> [9]. We assume that a considerable fraction of excitons and trions is scattered between the  $K^+$  and  $K^-$  valleys before exciton and trion recombination take place. With fast depolarization rates larger than  $1 \text{ ps}^{-1}$  for MoSe<sub>2</sub> monolayers under weak excitation conditions [52], the scattering process competes with or undercuts MoSe<sub>2</sub> exciton and trion lifetimes of about 2 ps and 15 ps, respectively [8, 46]. The dependence of the intensity difference on the degree of excitation polarization can directly be explained by the different initial population of the valleys. The imbalance between the two valleys rises as the degree of excitation polarization increases, which is reflected in larger intensity differences upon reversal of the magnetic field. Remarkably, the changes in exciton and trion populations observed in PL are thus a consequence of a spin-dependent tunneling process, even though any initial spin and valley polarization is lost well before exciton and trion recombination.

In summary, we have fabricated MoSe<sub>2</sub>/CGT heterostructures that reveal charge transfer from the MoSe<sub>2</sub> monolayer into the CGT, as predicted from the band alignment resulting from DFT calculations. The magnetization of the CGT flake and resultant spin-split density of states enables spin-dependent tunneling after nonresonant, circularly polarized excitation which manifests itself in altered exciton and trion intensities upon change of the external magnetic field direction. Intervalley scattering causes a loss of initial spin and valley polarization prior to exciton and trion recombination, resulting in an unpolarized collected PL. Our results underline the complex interplay of these competing processes on sub-picosecond timescales.

The observed effect holds significant promise for device applications. Circularly polarized excitation of our structures yields a helicity-dependent exciton/trion occupation imbalance which arises from spin-dependent tunneling. Consequently, the tunnel current itself depends on excitation helicity, potentially allowing for direct electrical readout of light helicity in suitably contacted heterostructures without the use of wave plates and polarizers to analyze the light polarization. A related concept was demonstrated recently using CrI<sub>3</sub> [53]. While the use of CGT with its low Curie temperature of about 60 K [23] limits applications, ferromagnetic behavior well above room temperature has been reported, e.g., in the layered ferromagnetic material Fe<sub>3</sub>GaTe<sub>2</sub> [54, 55]. Given the high remanence observed in this material, it may support the observed effect without the applied external magnetic field needed to align the magnetization in the case of CGT. Other relevant properties like its band alignment with MoSe<sub>2</sub> will require further investigation. With the rapid evolution of layered magnetic materials in recent years, other suitable alternatives to CGT are likely to emerge [56].

The observed effect relies neither on valley polarization nor on proximity-effect-induced valley Zeeman splitting and can thus be considered as rather robust. As our results demonstrate, nonresonant excitation yields a sizable occupation imbalance, indicating a spectrally broad range for helicity detection. Additionally, the picosecond timescales associated with the observed effect potentially enable ultrafast detector response times.

### III. METHODS

#### A. Sample fabrication

Under ambient conditions, hBN flakes and MoSe<sub>2</sub> monolayers were isolated from bulk crystals by mechanical exfoliation. The hBN flake was stamped with PDMS onto a Si/SiO<sub>2</sub> substrate via deterministic transfer [57]. A MoSe<sub>2</sub> monolayer was deposited on the hBN accordingly and afterwards annealed at about 180 °C in mild vacuum. CGT flakes were exfoliated from a bulk crystal (HQ graphene) under nitrogen atmosphere in a glovebox [58], thin flakes were thereby identified under an optical microscope based on their optical contrast. Immediately after exfoliation, the CGT flake was placed on top of the beforehand prepared hBN/MoSe<sub>2</sub> structure using a second deterministic stamping setup and PDMS transfer inside the glovebox. To protect the CGT from oxidation, the heterostructure was then fully encapsulated inside the glovebox by adding an hBN top layer.

## B. Optical measurements

### 1. Photoluminescence

For the PL measurements the sample was excited with a 1.96 eV continuous-wave diode laser focused to a spot size of about 1  $\mu\text{m}$  using an 80x microscope objective. The sample was mounted in a He-flow cryostat and cooled to a nominal temperature of about 5 K. To prevent sample heating, the excitation density was kept below 4 kW/cm<sup>2</sup>. The PL light emitted by the sample was collected using the same objective, filtered by long pass and analyzed with a combination of a spectrometer and a charge-coupled-device. To obtain PL maps of the sample the cryostat, with the sample inside, was moved in relation to the fixed laser spot through a computer-controlled xy stage. For helicity-resolved excitation, a linear polarizer and an achromatic quarter-wave plate ( $\lambda/4$ ) were placed in the excitation beam path. The wave plate was mounted in a motorized rotation stage, so that its angle could be varied automatically. Similarly, for helicity-resolved detection, an achromatic  $\lambda/4$ -plate and a linear polarizer (acting as an analyzer) were placed in the detection beam path in front of the spectrometer. For application of external magnetic fields, an air coil was placed around the cryostat, so that magnetic fields of up to 200 mT could be applied perpendicular to the sample plane. The current for the coil was supplied by a bipolar current source.

### 2. Polar magneto-optical Kerr effect

The polar MOKE measurements were performed in the setup described above using the 1.96 eV diode laser applying an excitation density of about 1 kW/cm<sup>2</sup>. All

measurements shown in the manuscript were performed at a nominal temperature of about 5 K. Laser intensity was modulated using a flywheel chopper. A beamsplitter cube was introduced into the detection beam path, so that the reflected laser light could be guided to an optical bridge detector with a pair of balanced photodiodes (see [59] for details). The difference signal from the photodiodes was detected using a lock-in amplifier. MOKE loops were measured by tracking the difference signal as a function of the applied magnetic field controlled by the bipolar current source.

## IV. ACKNOWLEDGEMENTS

The authors gratefully acknowledge technical assistance by E. Moldt and M. Kronseder, as well as fruitful discussions with R. Edhib. S. D. acknowledges financial support by the Humboldt foundation and a startup funding grant provided by the Deutsche Forschungsgemeinschaft (DFG, German Research Foundation) *via* SPP2244. T.K. acknowledges financial support by the DFG *via* the following grants: SFB1477 (project No. 441234705), SPP2244 (project No. 443361515), KO3612/7-1 (project No. 467549803) and KO3612/8-1 (project No. 549364913). K. Z. and J. F. acknowledge funding by the DFG *via* SFB 1277 (Project No. 314695032) and SPP 2244 (Project No. 443416183), as well as the European Union Horizon 2020 Research and Innovation Program under contract number 881603 (Graphene Flagship) and FLAGERA project 2DSOTECH. K.W. and T.T. acknowledge support from the JSPS KAKENHI (grant numbers 21H05233 and 23H02052) and World Premier International Research Center Initiative (WPI), MEXT, Japan.

- 
- [1] A. K. Geim and I. V. Grigorieva, Van der Waals heterostructures., *Nature* **499**, 419 (2013).
  - [2] K. F. Mak, C. Lee, J. Hone, J. Shan, and T. F. Heinz, Atomically thin MoS<sub>2</sub>: A new direct-gap semiconductor, *Phys. Rev. Lett.* **105**, 136805 (2010).
  - [3] D. Xiao, G. B. Liu, W. Feng, X. Xu, and W. Yao, Coupled spin and valley physics in monolayers of MoS<sub>2</sub> and other group-VI dichalcogenides, *Phys. Rev. Lett.* **108**, 196802 (2012).
  - [4] J. F. Sierra, J. Fabian, R. K. Kawakami, S. Roche, and S. O. Valenzuela, Van der waals heterostructures for spintronics and opto-spintronics, *Nature Nanotechnology* **16**, 856 (2021).
  - [5] J. R. Schaibley, H. Yu, G. Clark, P. Rivera, J. S. Ross, K. L. Seyler, W. Yao, and X. Xu, Valleytronics in 2D materials, *Nature Reviews Materials* **1**, 16055 (2016).
  - [6] K. F. Mak, K. He, J. Shan, and T. F. Heinz, Control of valley polarization in monolayer MoS<sub>2</sub> by optical helicity, *Nature Nanotechnology* **7**, 494 (2012).
  - [7] H. Zeng, J. Dai, W. Yao, D. Xiao, and X. Cui, Valley polarization in MoS<sub>2</sub> monolayers by optical pumping, *Nature Nanotechnology* **7**, 490 (2012).
  - [8] G. Wang, E. Palleau, T. Amand, S. Tongay, X. Marie, and B. Urbaszek, Polarization and time-resolved photoluminescence spectroscopy of excitons in MoSe<sub>2</sub> monolayers, *Applied Physics Letters* **106**, 112101 (2015).
  - [9] M. Baranowski, A. Surrente, D. K. Maude, M. Ballot, A. A. Mitroglu, P. C. M. Christianen, Y. C. Kung, D. Dumcenco, A. Kis, and P. Plochocka, Dark excitons and the elusive valley polarization in transition metal dichalcogenides, *2D Materials* **4**, 025016 (2017).
  - [10] H. Tornatzky, A.-M. Kaulitz, and J. Maultzsch, Resonance profiles of valley polarization in single-layer MoS<sub>2</sub> and MoSe<sub>2</sub>, *Phys. Rev. Lett.* **121**, 167401 (2018).
  - [11] D. MacNeill, C. Heikes, K. F. Mak, Z. Anderson, A. Kormányos, V. Zólyomi, J. Park, and D. C. Ralph, Breaking of valley degeneracy by magnetic field in monolayer MoSe<sub>2</sub>, *Phys. Rev. Lett.* **114**, 037401 (2015).
  - [12] A. Mitroglu, P. P. Plochocka-Maude, A. Granados del Aguila, P. C. M. Christianen, G. Deligeorgis, S. Anghel, L. Kulyuk, and D. K. Maude, Optical investigation of monolayer and bulk tungsten diselenide (WSe<sub>2</sub>) in high

- magnetic fields, *Nano Letters*, **15**, 150611125011005 (2015).
- [13] B. Scharf, G. Xu, A. Matos-Abiad, and I. Žutić, Magnetic proximity effects in transition-metal dichalcogenides: Converting excitons, *Phys. Rev. Lett.* **119**, 127403 (2017).
  - [14] D. Zhong, K. L. Seyler, X. Linpeng, R. Cheng, N. Sivadas, B. Huang, E. Schmidgall, T. Taniguchi, K. Watanabe, M. A. McGuire, W. Yao, D. Xiao, K.-M. C. Fu, and X. Xu, Van der waals engineering of ferromagnetic semiconductor heterostructures for spin and valleytronics, *Science Advances* **3**, e1603113 (2017).
  - [15] Y. Ye, J. Xiao, H. Wang, Z. Ye, H. Zhu, M. Zhao, Y. Wang, J. Zhao, X. Yin, and X. Zhang, Electrical generation and control of the valley carriers in a monolayer transition metal dichalcogenide, *Nature Nanotechnology* **11**, 598 (2016).
  - [16] H. Tornatzky, C. Robert, P. Renucci, B. Han, T. Blon, B. Lassagne, G. Ballon, Y. Lu, K. Watanabe, T. Taniguchi, B. Urbaszek, J. M. J. Lopes, and X. Marie, Spin dependent charge transfer in MoSe<sub>2</sub>/hBN/Ni hybrid structures, *Applied Physics Letters* **119**, 263103 (2021).
  - [17] C. Zhao, T. Norden, P. Zhang, P. Zhao, Y. Cheng, F. Sun, J. P. Parry, P. Taheri, J. Wang, Y. Yang, T. Scrace, K. Kang, S. Yang, G.-x. Miao, R. Sabirianov, G. Kioseoglou, W. Huang, A. Petrou, and H. Zeng, Enhanced valley splitting in monolayer WSe<sub>2</sub> due to magnetic exchange field, *Nature Nanotechnology* **12**, 757 (2017).
  - [18] K. F. Mak, J. Shan, and D. C. Ralph, Probing and controlling magnetic states in 2D layered magnetic materials, *Nature Reviews Physics* **1**, 646 (2019).
  - [19] S. Zhang, H. Wu, L. Yang, G. Zhang, Y. Xie, L. Zhang, W. Zhang, and H. Chang, Two-dimensional magnetic atomic crystals, *Mater. Horiz.* **9**, 559 (2022).
  - [20] T. P. Lyons, D. Gillard, A. Molina-Sánchez, A. Misra, F. Withers, P. S. Keatley, A. Kozikov, T. Taniguchi, K. Watanabe, K. S. Novoselov, J. Fernández-Rossier, and A. I. Tartakovskii, Interplay between spin proximity effect and charge-dependent exciton dynamics in MoSe<sub>2</sub>/CrBr<sub>3</sub> van der waals heterostructures, *Nature Communications* **11**, 6021 (2020).
  - [21] S. Rahman, B. Liu, B. Wang, Y. Tang, and Y. Lu, Giant photoluminescence enhancement and resonant charge transfer in atomically thin two-dimensional Cr<sub>2</sub>Ge<sub>2</sub>Te<sub>6</sub>/WS<sub>2</sub> heterostructures, *ACS Applied Materials & Interfaces* **13**, 7423 (2021).
  - [22] T. Zhang, S. Zhao, A. Wang, Z. Xiong, Y. Liu, M. Xi, S. Li, H. Lei, Z. V. Han, and F. Wang, Electrically and magnetically tunable valley polarization in monolayer MoSe<sub>2</sub> proximitized by a 2D ferromagnetic semiconductor, *Advanced Functional Materials* **32**, 2204779 (2022).
  - [23] C. Gong, L. Li, Z. Li, H. Ji, A. Stern, Y. Xia, T. Cao, W. Bao, C. Wang, Y. Wang, Z. Q. Qiu, R. J. Cava, S. G. Louie, J. Xia, and X. Zhang, Discovery of intrinsic ferromagnetism in two-dimensional van der waals crystals, *Nature* **546**, 265 (2017).
  - [24] Y. F. Li, W. Wang, W. Guo, C. Y. Gu, H. Y. Sun, L. He, J. Zhou, Z. B. Gu, Y. F. Nie, and X. Q. Pan, Electronic structure of ferromagnetic semiconductor CrGeTe<sub>3</sub> by angle-resolved photoemission spectroscopy, *Phys. Rev. B* **98**, 125127 (2018).
  - [25] See Supplemental Material at for additional experimental results and details of DFT calculations.
  - [26] H. Fang, C. Battaglia, C. Carraro, S. Nemsak, B. Ozdol, J. S. Kang, H. A. Bechtel, S. B. Desai, F. Kronast, A. A. Unal, G. Conti, C. Conlon, G. K. Palsson, M. C. Martin, A. M. Minor, C. S. Fadley, E. Yablonovitch, R. Maboudian, and A. Javey, Strong interlayer coupling in van der waals heterostructures built from single-layer chalcogenides, *Proceedings of the National Academy of Sciences* **111**, 6198 (2014).
  - [27] A. Vervelaki, K. Bagani, D. Jetter, M.-H. Doan, T. K. Chau, B. Gross, D. V. Christensen, P. Bøggild, and M. Poggio, Visualizing thickness-dependent magnetic textures in few-layer Cr<sub>2</sub>Ge<sub>2</sub>Te<sub>6</sub>, *Communications Materials* **5**, 1 (2024).
  - [28] A. Noah, H. Alpern, S. Singh, A. Gutfreund, G. Zisman, T. D. Feld, A. Vakahi, S. Remennik, Y. Paltiel, M. E. Huber, V. Barrena, H. Suderow, H. Steinberg, O. Millo, and Y. Anahory, Interior and edge magnetization in thin exfoliated CrGeTe<sub>3</sub> films, *Nano Letters* **22**, 3165 (2022).
  - [29] K. Zollner, P. E. Faria Junior, and J. Fabian, Proximity exchange effects in MoSe<sub>2</sub> and WSe<sub>2</sub> heterostructures with CrI<sub>3</sub>: Twist angle, layer, and gate dependence, *Physical Review B* **100**, 085128 (2019).
  - [30] K. Zollner, P. E. Faria Junior, and J. Fabian, Strong manipulation of the valley splitting upon twisting and gating in MoSe<sub>2</sub>/CrI<sub>3</sub> and WSe<sub>2</sub>/CrI<sub>3</sub> van der waals heterostructures, *Physical Review B* **107**, 035112 (2023).
  - [31] S. R. Bahn and K. W. Jacobsen, An object-oriented scripting interface to a legacy electronic structure code, *Comput. Sci. Eng.* **4**, 56 (2002).
  - [32] P. Lazic, Cellmatch: Combining two unit cells into a common supercell with minimal strain, *Computer Physics Communications* **197**, 324 (2015).
  - [33] D. S. Koda, F. Bechstedt, M. Marques, and L. K. Teles, Coincidence lattices of 2D crystals: heterostructure predictions and applications, *The Journal of Physical Chemistry C* **120**, 10895 (2016).
  - [34] S. Carr, S. Fang, and E. Kaxiras, Electronic-structure methods for twisted moiré layers, *Nature Reviews Materials* **5**, 748 (2020).
  - [35] V. Carteaux, D. Brunet, G. Ouvrard, and G. Andre, Crystallographic, magnetic and electronic structures of a new layered ferromagnetic compound Cr<sub>2</sub>Ge<sub>2</sub>Te<sub>6</sub>, *J. Phys.: Condens. Mat.* **7**, 69 (1995).
  - [36] W. J. Schutte, J. L. De Boer, and F. Jellinek, Crystal structures of tungsten disulfide and diselenide, *Journal of Solid State Chemistry* **70**, 207 (1987).
  - [37] P. Hohenberg and W. Kohn, Inhomogeneous electron gas, *Phys. Rev.* **136**, B864 (1964).
  - [38] P. Giannozzi and et al., Quantum espresso: a modular and open-source software project for quantum simulations of materials, *J. Phys.: Cond. Mat.* **21**, 395502 (2009).
  - [39] G. Kresse and D. Joubert, From ultrasoft pseudopotentials to the projector augmented-wave method, *Phys. Rev. B* **59**, 1758 (1999).
  - [40] J. P. Perdew, K. Burke, and M. Ernzerhof, Generalized gradient approximation made simple, *Phys. Rev. Lett.* **77**, 3865 (1996).
  - [41] S. Grimme, Semiempirical gga-type density functional constructed with a long-range dispersion correction, *J. Comput. Chem.* **27**, 1787 (2006).
  - [42] S. Grimme, J. Antony, S. Ehrlich, and H. Krieg, A consistent and accurate ab initio parametrization of density functional dispersion correction (DFT-D) for the 94 elements H-Pu, *J. Chem. Phys.* **132**, 154104 (2010).
  - [43] V. Barone, M. Casarin, D. Forrer, M. Pavone, M. Sami, and A. Vittadini, Role and effective treatment of dispersive forces in materials: Polyethylene and graphite crystals

- as test cases, *J. Comput. Chem.* **30**, 934 (2009).
- [44] K. F. Mak, K. He, C. Lee, G. H. Lee, J. Hone, T. F. Heinz, and J. Shan, Tightly bound trions in monolayer  $\text{MoS}_2$ , *Nature Materials* **12**, 207 (2012).
  - [45] Y. Liu, T. Shen, S. Linghu, R. Zhu, and F. Gu, Electrostatic control of photoluminescence from A and B excitons in monolayer molybdenum disulfide, *Nanoscale Advances* **4**, 2484 (2022).
  - [46] C. Robert, D. Lagarde, F. Cadiz, G. Wang, B. Lasagne, T. Amand, A. Balocchi, P. Renucci, S. Tongay, B. Urbaszek, and X. Marie, Exciton radiative lifetime in transition metal dichalcogenide monolayers, *Phys. Rev. B* **93**, 205423 (2016).
  - [47] X. Hong, J. Kim, S.-F. Shi, Y. Zhang, C. Jin, Y. Sun, S. Tongay, J. Wu, Y. Zhang, and F. Wang, Ultrafast charge transfer in atomically thin  $\text{MoS}_2/\text{WS}_2$  heterostructures, *Nature Nanotechnology* **9**, 682 (2014).
  - [48] C. Jin, E. Y. Ma, O. Karni, E. C. Regan, F. Wang, and T. F. Heinz, Ultrafast dynamics in van der waals heterostructures, *Nature Nanotechnology* **13**, 994 (2018).
  - [49] P. Steinleitner, P. Merkl, P. Nagler, J. Mornhinweg, C. Schüller, T. Korn, A. Chernikov, and R. Huber, Direct observation of ultrafast exciton formation in a monolayer of  $\text{WSe}_2$ , *Nano Letters* **17**, 1455 (2017).
  - [50] A. Singh, G. Moody, K. Tran, M. E. Scott, V. Overbeck, G. Berghäuser, J. Schaibley, E. J. Seifert, D. Pleskot, N. M. Gabor, J. Yan, D. G. Mandrus, M. Richter, E. Malic, X. Xu, and X. Li, Trion formation dynamics in monolayer transition metal dichalcogenides, *Physical Review B* **93**, 041401 (2016).
  - [51] M. M. Glazov, T. Amand, X. Marie, D. Lagarde, L. Bouet, and B. Urbaszek, Exciton fine structure and spin decoherence in monolayers of transition metal dichalcogenides, *Physical Review B* **89**, 201302 (2014).
  - [52] F. Mahmood, Z. Alpichshev, Y.-H. Lee, J. Kong, and N. Gedik, Observation of exciton–exciton interaction mediated valley depolarization in monolayer  $\text{MoS}_2$ , *Nano Letters* **18**, 223 (2017).
  - [53] X. Cheng, Z. Cheng, C. Wang, M. Li, P. Gu, S. Yang, Y. Li, K. Watanabe, T. Taniguchi, W. Ji, and L. Dai, Light helicity detector based on 2D magnetic semiconductor  $\text{CrI}_3$ , *Nature Communications* **12**, 1 (2021).
  - [54] G. Zhang, F. Guo, H. Wu, X. Wen, L. Yang, W. Jin, W. Zhang, and H. Chang, Above-room-temperature strong intrinsic ferromagnetism in 2D van der waals  $\text{Fe}_3\text{GaTe}_2$  with large perpendicular magnetic anisotropy, *Nature Communications* **13**, 5067 (2022).
  - [55] S. Wu, Z. He, M. Gu, L. Ren, J. Li, B. Deng, D. Wang, X. Guo, W. Li, M. Chen, Y. Chen, M. Meng, Q. Ye, B. Shen, X. Chen, J. Guo, G. Xing, I. K. Sou, and S. Li, Robust ferromagnetism in wafer-scale  $\text{Fe}_3\text{GaTe}_2$  above room-temperature, *Nature Communications* **15**, 10765 (2024).
  - [56] B. Zhang, P. Lu, R. Tabrizian, P. X.-L. Feng, and Y. Wu, 2D magnetic heterostructures: spintronics and quantum future, *npj Spintronics* **2**, 6 (2024).
  - [57] A. Castellanos-Gomez, M. Buscema, R. Molenaar, V. Singh, L. Janssen, H. S. J. van der Zant, and G. A. Steele, Deterministic transfer of two-dimensional materials by all-dry viscoelastic stamping, *2D Materials* **1**, 011002 (2014).
  - [58] P. Gant, F. Carrascoso, Q. Zhao, Y. K. Ryu, M. Seitz, F. Prins, R. Frisenda, and A. Castellanos-Gomez, A system for the deterministic transfer of 2D materials under inert environmental conditions, *2D Materials* **7**, 025034 (2020).
  - [59] M. Kempf, A. Schubert, R. Schwartz, and T. Korn, Two-color Kerr microscopy of two-dimensional materials with sub-picosecond time resolution, *Review of Scientific Instruments* **92**, 113904 (2021).